



Radiation dose distribution of liquid fueled thorium molten salt reactor

Chang-Yuan Li^{1,2} · Xiao-Bin Xia² · Jun Cai² · Zhi-Hong Zhang² · Guo-Qing Zhang³ · Jian-Hua Wang² · Zhi-Cheng Qian²

Received: 29 September 2020 / Revised: 25 November 2020 / Accepted: 27 November 2020 / Published online: 25 February 2021
© China Science Publishing & Media Ltd. (Science Press), Shanghai Institute of Applied Physics, the Chinese Academy of Sciences, Chinese Nuclear Society 2021

Abstract A liquid fueled thorium molten salt reactor (TMSR-LF), one of the Generation IV reactors, was designed by the Shanghai Institute of Applied Physics, Chinese Academy of Sciences. This study uses the *rt* code to calculate the neutron and gamma dose rate distributions around the reactor. Multiple types of tallies and variance reduction techniques were employed to reduce calculation time and obtain convergent calculation results. Based on the calculation and analysis results, the TMSR-LF1 radiation shield with a 60-cm serpentine concrete layer and a 120-cm ordinary concrete layer is able to meet radiation requirements. The gamma dose rate outside the reactor biological shield was 16.1 mSv h^{-1} ; this is higher than the neutron dose rate of $3.71 \times 10^{-2} \text{ mSv h}^{-1}$. The maximum thermal neutron flux density outside the reactor biological shield was $1.89 \times 10^3 \text{ cm}^{-2} \text{ s}^{-1}$, which was below the $1 \times 10^5 \text{ cm}^{-2} \text{ s}^{-1}$ limit.

Keywords Liquid fueled · Molten salt reactor · Neutron and gamma · Dose rate

1 Introduction

The Generation IV International Forum categorized molten salt reactor (MSR) as a Generation IV reactor due to its numerous advantages like good neutron economy, inherent safety, online reprocessing, reduced production of radioactive waste, and nuclear non-proliferation [1–3]. In 2011, the Chinese Academy of Sciences launched a thorium MSR project and established a research center at the Shanghai Institute of Applied Physics. This project focused on the development of a liquid fueled thorium molten salt reactor (TMSR-LF1). The TMSR-LF1 is the first research reactor with a thermal power design of 2 MW, using $\text{LiF-BeF}_2\text{-ZrF}_4\text{-UF}_4$ as its fuel and primary coolant. Fuel dissolved in molten salt coolant is a representative characteristic compared to traditional reactors [4, 5].

As a fission reactor, the TMSR-LF1 is a strong source of neutrons and gamma radiation during operation and even following shutdown. The radiation dose of TMSR-LF1 is mainly sourced from the neutron and gamma rays produced by the fission of fuels in the reactor core and by the decay of fission products [6]. Therefore, radiation dose distribution around the reactor is important, for shielding design and radiation protection. To protect people and equipment from radiation damage, the selection of a suitable shielding material and optimization of the shielding structure are necessary in shielding design. The TMSR-LF1 biological shield is composed of a serpentine concrete shield and an ordinary concrete shield. A 60-cm serpentine concrete layer was used inside ordinary concrete to reduce the neutron and photon energy flux densities to protect the ordinary concrete structure. The reactor neutron and gamma dose rate distributions inside and outside the reactor shield have been calculated using the Monte Carlo

This work was supported by the Chinese Academy of Sciences TMSR Strategic Pioneer Science and Technology Project (No. XDA02010000).

✉ Xiao-Bin Xia
xiaxiaobin@sinap.ac.cn

¹ University of Chinese Academy of Sciences, Beijing 100049, China

² Shanghai Institute of Applied Physics, Chinese Academy of Sciences, Shanghai 201800, China

³ Siemens Shanghai Medical Equipment Ltd., Shanghai 201318, China

N-Particle Transport (MCNP) code. Within the biological shielding layer of the reactor, the neutron dose rate is higher than the gamma dose rate. As neutrons generate many secondary gamma rays when they are moderated and absorbed in the concrete shield, the gamma dose rate outside the reactor concrete shielding layer was higher than the neutron dose rate. To limit the radiation effects of thermal neutron activation products in the areas where personnel need entry following the shutdown of the reactor, the thermal neutron flux density should be less than $1 \times 10^5 \text{ cm}^{-2} \text{ s}^{-1}$ during normal operating conditions. Based on the results, the thermal neutron flux density outside the concrete shield layers of TMSR-LF1 meets this requirement.

2 Calculation methods and models

The widely used methods for shielding calculation of reactors are the discrete ordinate (SN) method and the Monte Carlo (MC) method [7, 8]. The shielding calculation of the TMSR-LF1 uses the MCNP5 code. This is based on the MC method, which may be used to theoretically duplicate a statistical process (such as the interaction of nuclear particles with materials). This code is particularly useful for complex problems that cannot be modeled by computer codes that use deterministic methods. MCNP5 was developed at the Los Alamos National Laboratory and is applicable to neutrons, photons, electrons, and coupled neutron/photon/electron transportation. For its ability to deal with complex three-dimensional (3D) geometry, a rich set of integrated variance reduction techniques and the support for parallel computing have been widely used in shielding design [9].

There are some differences in the TMSR-LF1 compared to solid fuel reactors [10]. For example, the coolant temperature exceeds 600 °C, the power density is high in the reactor core, and molten salt is used as coolant; these features have introduced significant challenges to shielding design. TMSR-LF1 uses serpentine concrete as the heat shield as it possesses excellent heat resistance and has no strict requirements regarding the irradiation environment [11, 12]. The entire reactor cabin is divided into upper and lower regions by a 30-cm steel plate. The reactor core is located in the lower part of the reactor cabin, and the control rod drive motor, main pump drive motor, and measurement equipment are located in the upper region of the reactor cabin. The side shielding system in the lower region of the TMSR-LF1 consists of a 60-cm serpentine concrete shield layer and a 120-cm ordinary concrete shield layer. The bottom shielding system of the lower region consists of a 40-cm serpentine concrete shield layer and a 120-cm ordinary concrete shield layer. The side shielding

system of the upper region of the TMSR-LF1 consists of a 120-cm ordinary concrete shield layer, and the top shielding system of the upper region consists of a 180-cm ordinary concrete shield layer. Table 1 details the additional design parameters.

The TMSR-LF1 reactor has a relatively compact core composed of a fuel region and graphite reflector. The reactor, including the 3-cm thickness reactor vessel, has a diameter of 237 cm and is 320 cm in height. The active region containing the graphite reflector is 230 cm in diameter and 180 cm in height. The fuel region, a hexagonal prism, is located in the center of the active region; this region contains 244 fuel channels that are 4 cm in diameter, where the center distance between adjacent channels is 10 cm. Above the fuel region is a 12-cm compressed steel plate made of Hastelloy-N and a 62.6-cm high covering gas region. Below the fuel region, is a support steel plate made of Hastelloy-N with an 8 cm thickness, a fuel chamber that is 10 cm in height, and an ellipsoidal graphite reflective layer that had a maximum thickness of approximately 40 cm. The reactor vessel is made of Hastelloy-N and is 3 cm in thickness [13]. The primary loop heat exchanger was placed in the reactor to reduce the radiation effect of the primary loop radioactivity. A 3D simulation model was constructed, based on the design parameters of TMSR-LF1, as shown in Fig. 1. Then, the MCNP5 code was used to conduct coupled neutron/gamma transport.

2.1 Neutron emission rate of reactor

The MCNP5 code provides the statistical average dose probability distribution per neutron by tracking neutrons and neutron-induced gamma rays. The final calculated dose rate is the statistical average multiplied by the neutron emission rate of the reactor. The neutron emission rate of the reactor is largely dependent on the thermal power of the reactor. As the thermal power of TMSR-LF1 is 2 MW, the number of neutrons released per second may be calculated using two methods. The first method uses theory calculation with Formula (1) [14, 15], while the second method calculates the average energy deposition of one neutron in the reactor core cell using the MCNP5 code [16]. Then, the number of neutrons released per second of the reactor core based on reactor power may be derived by Formula (2) [17]:

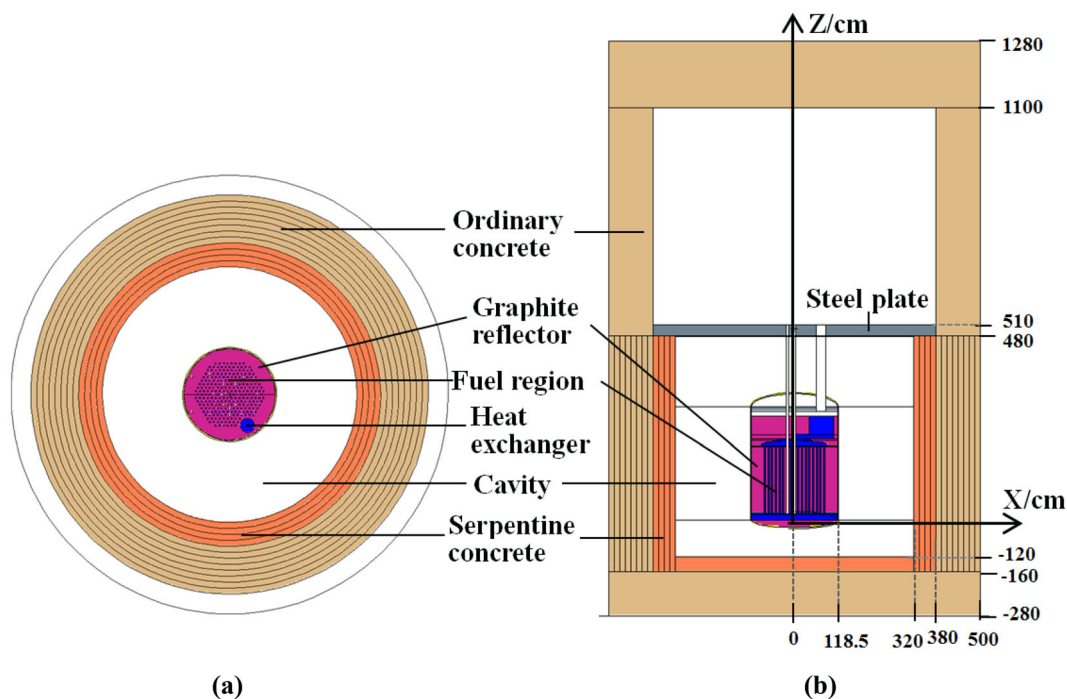
$$N = \frac{P}{E} \times n = \frac{2 \text{ MW}}{190 \text{ MeV}} \times 2.42 \approx 1.60 \times 10^{17} \text{ neutrons/s}, \quad (1)$$

$$N = \frac{P}{\varepsilon} = \frac{2 \text{ MW}}{80.13 \text{ MeV}} \approx 1.56 \times 10^{17} \text{ neutrons/s}, \quad (2)$$

where N is the number of neutrons released per second in the reactor core; E is the energy released by one ^{235}U

Table 1 TMSR-LF1 parameters

Parameter	Specification
Thermal power	2 MW
Fuel and coolant	LiF-BeF ₂ -ZrF ₄ -UF ₄ (65.30-28.71-4.79-1.20 mol%)
Fuel ²³⁵ U enrichment	19.75%
⁷ Li abundance	99.95 atom%
Coolant inlet temperature	630 °C
Coolant outlet temperature	650 °C
Reactor fuel region diameter/height	234/180 cm
Serpentine concrete inner diameter/thickness	640/60 cm
Serpentine concrete density	2.26 g/cm ³
Serpentine concrete chemical composition	SiO ₂ -MgO-CaO-Al ₂ O ₃ -Fe ₂ O ₃ -H ₂ O (33.47-28.58-14.20-5.3-4.9-13.55 wt.%)
Ordinary concrete inner diameter/thickness	760/120 cm
Ordinary concrete density	2.30 g/cm ³

**Fig. 1** (Color online) TMSR-LF1 model in MCNP. **a** Top view; **b** front view

fission (~ 190 meV excluding the energy of the neutrino); n is the number of neutrons produced by one ²³⁵U fission (i.e., 2.42 [14]); and ϵ is the average energy deposition of one neutron in the reactor core calculated by MCNP5 code using the detector of energy deposition tally F6: NP (i.e., 80.13 meV). These two methods produce very similar results, demonstrating that both methods are applicable. On a conservative basis, the number of neutrons released per second of 2 MW TMSR-LF1 was adopted as 1.60×10^{17} neutrons/s.

When the reactor is in a shutdown scenario, the radionuclides in the reactor core continue to produce radiation effects during the decay process. At the end of life for the TMSR-LF1, the number of gamma released per second by the reactor core fission products and activation products was approximately $7.02 \times 10^{17} \text{ s}^{-1}$ at the zero moment of reactor shutdown. The gamma emission rate was reduced to $2.35 \times 10^{16} \text{ s}^{-1}$ following 12 d of reactor shutdown attenuation. These data were calculated using the ORIGEN-S code. This code is the depletion and decay module in the SCALE code system and has been widely

used in nuclear reactor and processing plant design studies, spent fuel transportation and storage studies, burnup credit evaluations, decay heat and radiation safety analyses, and environmental assessments [18]. The TMSR-LF1 fuel salt contains a large amount of ^9Be ; the neutrons are produced by the (α, n) between alpha particles with ^9Be and are produced by the (γ, n) between gamma rays with ^9Be [19–21]. The number of neutrons released per second by (α, n) and (γ, n) is approximately 3.15×10^{15} neutrons/s at the zero moment of the shutdown scenario, and the neutron emission rate was reduced to $2.46 \times 10^{12} \text{ s}^{-1}$ following 12 d of reactor shutdown attenuation [22]. The radiation impact of neutrons and gamma for the reactor shutdown scenario is much smaller than the radiation impact during reactor operation. The fuel salt is discharged into the fuel salt tank located underground following 12 d of cooling decay [23]. Therefore, the radiation dose impact for the TMSR-LF1 reactor shutdown scenario may be ignored compared to the radiation impact during reactor operation.

2.2 Spectra of neutron and gamma

The neutron and gamma energy spectra are the premise of analyzing the radiation dose distribution of neutrons and gamma rays. The neutron and gamma energy spectra may be used to predict the dose distribution in advance and provide guidance to select suitable shielding materials. The energy spectrum of neutrons produced by ^{235}U fission in the reactor core follows the Maxwell–Boltzmann distribution after being sufficiently moderated by graphite [24, 25]. The peak of the neutron energy spectrum of the reactor core is related to the moderator and the reactor core temperature. The neutron energy after completely slowing down may be derived using Formula (3):

$$E_{kT} = k \times T \approx 7.78 \times 10^{-2} \text{ eV}, \quad (3)$$

where E_{kT} is the neutron energy after being sufficiently moderated; k is the Boltzmann constant (i.e., $8.62 \times 10^{-5} \text{ eV/K}$); and T is the temperature of the graphite moderator in the reactor core (903 K). The theoretical calculation of the TMSR-LF1 core neutron energy should be $7.78 \times 10^{-2} \text{ eV}$ after being sufficiently moderated.

TMSR-LF1 is a thermal neutron reactor, as such, the spectra of neutron and gamma shown in Fig. 2 were calculated with the MCNP5 code using the ring detector tally F5. The maximum neutron flux density was approximately $2.2 \times 10^{13} \text{ cm}^{-2} \text{ s}^{-1}$ in the reactor core fuel region and approximately $2.6 \times 10^{11} \text{ cm}^{-2} \text{ s}^{-1}$ outside the reactor vessel. The maximum gamma flux density was approximately $8.4 \times 10^{12} \text{ cm}^{-2} \text{ s}^{-1}$ in the reactor core fuel region and approximately $1.9 \times 10^{11} \text{ cm}^{-2} \text{ s}^{-1}$ outside the reactor vessel.

The neutron spectrum with energy ranging from 10^{-9} to 10 meV was divided into 100 energy groups using geometric progression. The gamma spectrum with energy ranging from 0 to 5 meV was divided into 50 energy groups using arithmetic progression. The computational variances of each neutron and gamma energy groups were less than 5% when the number of neutron histories was 2×10^8 .

The peak of the neutron spectrum of ^{235}U fission was approximately 2 meV, and the peak of the neutron spectrum in the reactor core fuel area was approximately 10^{-7} meV following graphite moderation. This was slightly larger than the theoretical results of formula (3) (i.e., $7.78 \times 10^{-8} \text{ meV}$). The percentage of neutrons in this energy segment had lowered, and the percentage of neutrons in the high-energy segments had increased outside the reactor vessel. The peak of gamma spectrum in the reactor core fuel area was approximately 0.25 meV, and the gamma spectrum had become “harder” outside of the reactor vessel as the gamma with low energy rapidly reduces relative to the high-energy gamma when it travels through the graphite reflector and reactor vessel.

2.3 Variance reduction techniques

The surface detector tally F2 and the ring detector tally F5 have been used to calculate the dose rate outside the biological shield. It is necessary for the shielding calculation of TMSR-LF1 to solve the deep penetration problem as a result of the thick concrete shield. Two calculation techniques were used together to reduce calculation variance and obtain convergent calculation results. The first was the Surface Source Write Card (SSW) used to generate a surface radioactive source. The second technique was the Weight Window Generation Card (WWG) used to estimate the importance of the space-energy regions of phase space. The calculation process may be divided into four steps:

1. Creation of an elaborate TMSR-LF1 core model, and use of the nuclear criticality (KCODE) card, where SSW produces a KCODE nuclear criticality surface source file for use in subsequent MCNP calculations;
2. Replacement of the KCODE nuclear criticality source card with the general source card, use of a fission turnoff card to turn off fission in the reactor core, and use of the Surface Source Read Card to read the nuclear criticality surface source file to continue the calculation;
3. Use of the WWG to estimate the importance of the space-energy regions of the phase space and produce a weight window file;
4. Use of the importance function written on the weight window cards (WWE:N, WWE:P); we replaced the

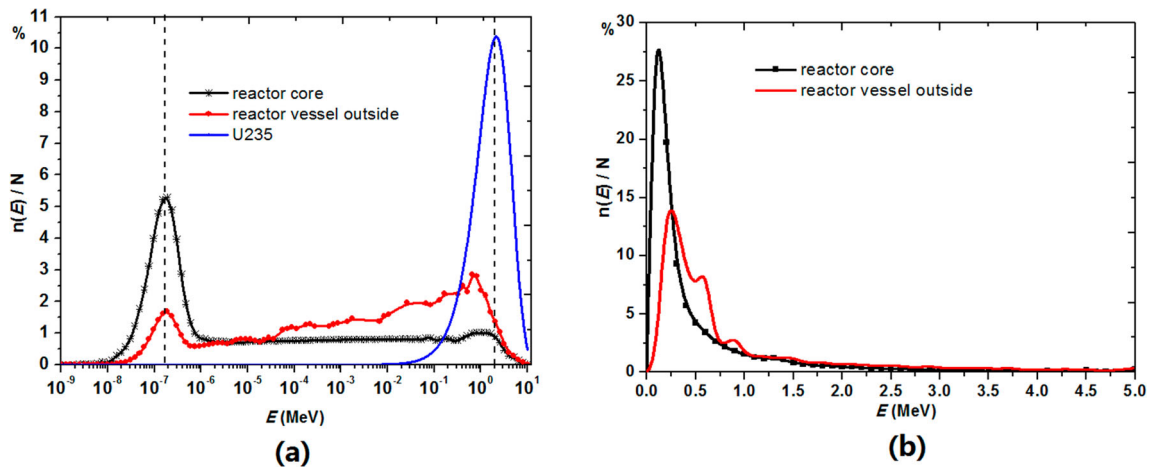


Fig. 2 (Color online) Energy distribution spectrum of neutrons and gamma. **a** Neutron; **b** gamma

neutron and photon importance (IMP:N,IMP:P) in the calculation model card and continued the calculation.

3 Results and discussion

The radial flux density distribution of neutrons and gamma around the reactor was calculated by the MCNP5 code using the Mesh-Based Weight Window Generator (MESH) and the track-length detector tally F4; the latter is referred to as the Superimposed Mesh Tally (FMESH). The radial dose rate distribution of neutrons and gamma around the reactor was converted from the flux density distribution by using flux-to-dose conversion factors recommended in the International Symposium on the System of Radiological Protection (ICRP) Publication 74 [26, 27]. By graphically displaying the calculation results of FMESH, the dose rate distribution of neutrons and gamma may be reflected more intuitively. The dose rate distribution of neutrons and gamma around the reactor is shown in Fig. 3a and b, respectively. The neutron dose rate in the reactor core was higher than 1×10^9 mSv/h, while the gamma dose rate was lower than 1×10^8 mSv/h. Figure 3 shows that the neutron dose rate was higher than the gamma dose rate in the reactor core and around the reactor vessel, while the gamma dose rate is higher than the neutron dose rate outside the concrete shield. The minimum neutron dose rate in the lower region of the reactor cabin exceeded 1×10^6 mSv/h, while the minimum gamma dose rate exceeded 1×10^5 mSv/h. The maximum neutron dose rate in the upper region of the reactor cabin was lower than 1×10^6 mSv/h, while the maximum gamma dose rate was lower than 1×10^4 mSv/h. The 30-cm shielding steel plate between the upper and lower regions of the reactor cabin is

able to effectively reduce the radiation dose rate of the upper region, particularly for the gamma dose rate.

If the number of simulated particles was below 5×10^8 , the number of particles counted in the outer concrete was limited, and the variance of the calculated data for the outermost layer of ordinary concrete exceeded 5% using the detector tally F4. As such, irregular jagged colors appeared in the outer boundary area of the ordinary concrete in Fig. 3. The radiation dose distribution outside the concrete shielding layer, particularly at the top of the reactor, was not well represented using FMESH4. The SSW Card and WWG Card were used to reduce variance. This was during the calculation of radiation dose rates with varied concrete shield thicknesses using the surface detector tally F2 and ring detector tally F5. The calculation process is described in detail below using the example of the radiation dose rate distribution in serpentine concrete and ordinary concrete on the side of the reactor cabin. The tally segment card FS2 was used to intercept the concrete layer on the side of the reactor into upper, middle, and lower regions with the upper and bottom of the reactor fuel as the boundary during the calculation of tally F2 (Fig. 4). Section II provides the details of the calculation process and steps. When the number of simulated particles was $5E + 8$, the variances of all calculated data were less than 5% based on the combined used of SSW and WWG.

The serpentine concrete on the side of the reactor was divided into four layers, and the ordinary concrete was divided into eight layers, each with a thickness of 15 cm. Tally F2 calculated the average dose rate of the surface, while the calculation using tally F5 selected the same height position to the center of the reactor fuel area. The radiation dose rate distribution in serpentine concrete and ordinary concrete was given by calculating the neutron and gamma dose rates corresponding to different concrete thicknesses (Fig. 4). The equations for the gamma dose

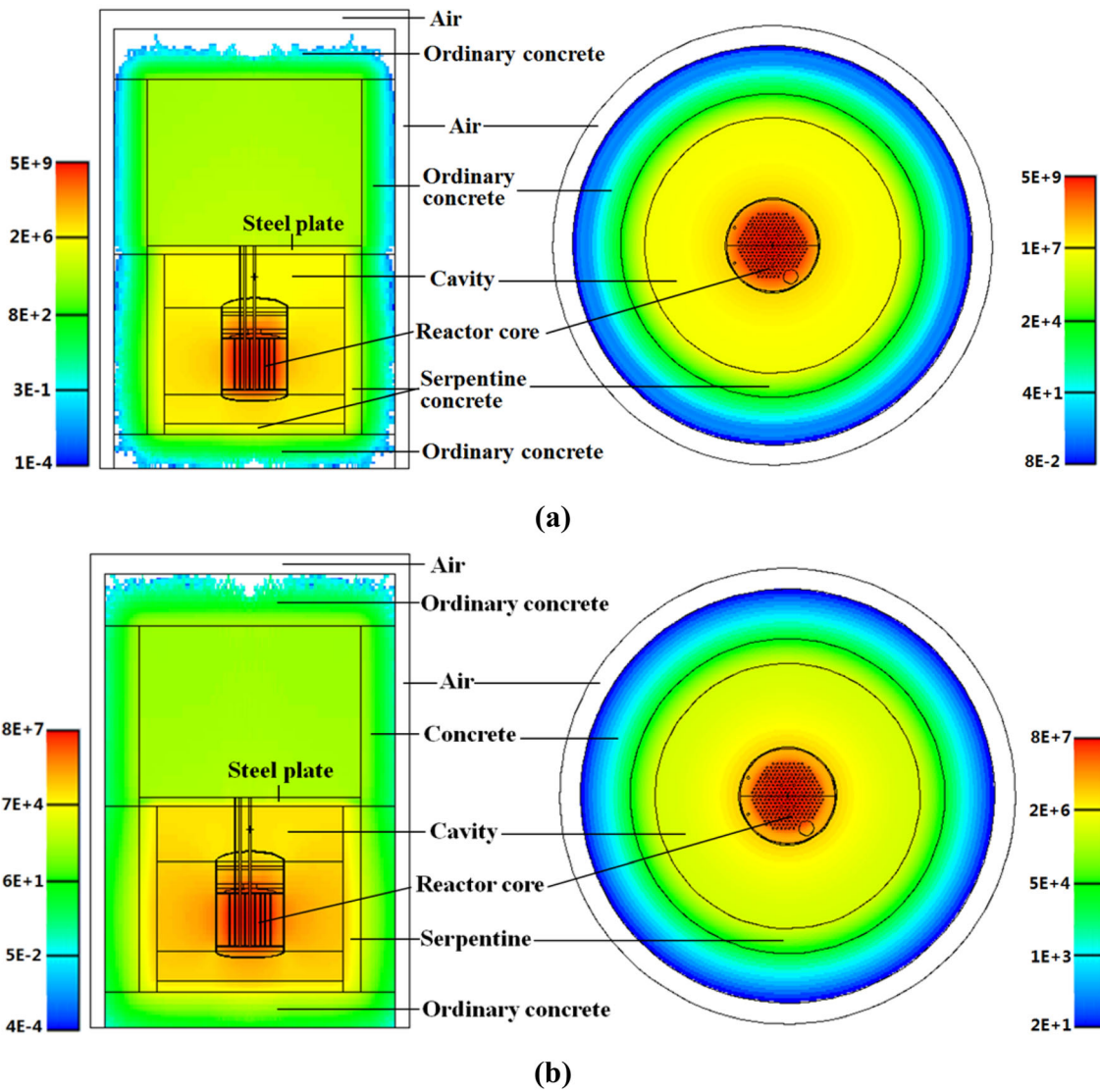


Fig. 3 (Color online) Dose rate distribution of neutrons and gamma around the reactor (mSv/h). **a** Neutron; **b** gamma

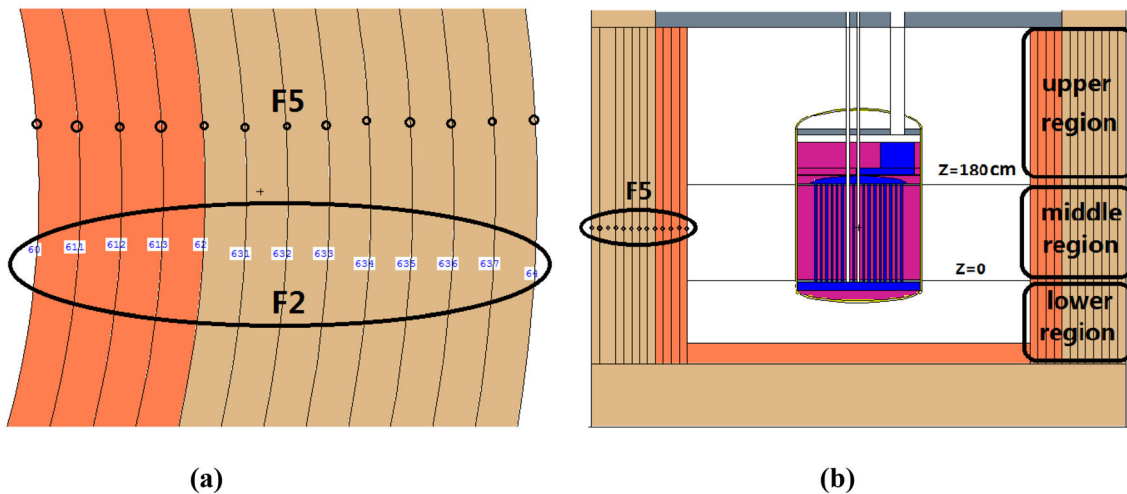


Fig. 4 (Color online) Biological shield and tallies. **a** Top view and enlarged view of tallies. **b** Front view

rate as a function of serpentine thickness, calculated using tally F2 in the upper, middle, and lower regions on the side of the reactor were Formulas (4, 5, 6), respectively. The equation for gamma dose rate as a function of serpentine thickness calculated using tally F5 was Formula (7):

$$D_{\text{upper}} = 6.64 \times 10^5 \exp(-0.065x) \text{ mSv/h}, \quad (4)$$

$$D_{\text{middle}} = 1.17 \times 10^6 \exp(-0.063x) \text{ mSv/h}, \quad (5)$$

$$D_{\text{lower}} = 7.05 \times 10^5 \exp(-0.062x) \text{ mSv/h}, \quad (6)$$

$$D_{\text{F5}} = 1.21 \times 10^6 \exp(-0.063x) \text{ mSv/h}, \quad (7)$$

where x is the thickness of serpentine concrete (cm); D_{upper} is the gamma dose rate of the upper region on the side of the reactor, where the correlation factor (R^2) of Formula (4) was 0.9993; D_{middle} is the gamma dose rate of the middle region on the side of the reactor, where the R^2 of Formula (5) was 0.9977; D_{lower} is the gamma dose rate of the lower region on the side of the reactor, where the R^2 of Formula (6) was 0.9977; and D_{F5} is the gamma dose rate of the same height position to the center of the reactor fuel area on the side of the reactor, where the R^2 of Formula (7) was 0.9998. The gamma dose rate on the side of the reactor showed a good exponential relationship with the thickness of the serpentine concrete with an $R^2 > 0.99$ [28]. Based on formula (4–7), the 10th-value layer thickness of the gamma dose rate on the side of the serpentine concrete was 35–38 cm.

The dose rate in the middle region facing the reactor fuel was higher than the dose rate in the upper and lower regions. The results using the F2 and F5 tallies were relatively close. The calculated data using F5 were slightly larger than F2 as the radiation dose levels in the center of the reactor active area were higher than those in the upper and lower regions. Increasing the number of F5 detectors reduced the statistical efficiency of the MCNP code, whereby the variance of the F5 calculation result was greater than the F2 result [29]. Therefore, the calculation data of the middle region using tally F2 were selected as the result for neutron and gamma radiation dose distribution. Formula (8) shows that the neutron dose rates vary with the serpentine concrete shield thickness as fitted with the surface detector tally F2 results.

$$D_{\text{neutron}} = 6.56 \times 10^6 \exp(-0.112x) \text{ mSv/h}, \quad (8)$$

In this formula, D_{neutron} is the neutron dose rate of the middle region on the side of the reactor; x is the thickness of serpentine concrete, where the R^2 of Formula (8) was 0.9997. The neutron dose rate in serpentine concrete was higher than the gamma dose rate. However, the neutron dose rate decline with increased serpentine concrete thickness was more rapid than the gamma dose rate.

The gamma and neutron dose rates varied with ordinary concrete shield thickness on the side of the reactor fitted with the surface detector; the tally F2 results are shown in Formulas (9, 10). In these formulas, x is the thickness of serpentine concrete (e.g., 60 cm); y is the thickness of the ordinary concrete (0–120 cm); D_{gamma} is the gamma dose rate of the middle region on the side of the reactor, where the R^2 of Formula (9) was 0.9998; D_{neutron} is the neutron dose rate of the middle region on the side of the reactor, where the R^2 of Formula (10) was 0.9996. There was a good fit between the exponential formula of gamma and neutron dose rates with ordinary concrete thickness. The neutron dose rate in ordinary concrete was lower than the gamma dose rate, and the neutron dose rate decline with ordinary concrete was more than the decline of the gamma dose rate.

$$\begin{aligned} D_{\text{gamma}} &= 1.17 \times 10^6 \exp(-0.063x) \times \exp(-0.061y) \\ &= 2.67 \times 10^4 \exp(-0.061y) \text{ mSv/h}, \end{aligned} \quad (9)$$

$$\begin{aligned} D_{\text{neutron}} &= 6.56 \times 10^6 \exp(-0.112x) \times \exp(-0.094y) \\ &= 7.91 \times 10^3 \exp(-0.094y) \text{ mSv/h}, \end{aligned} \quad (10)$$

3.1 Distribution of neutron flux density

Reactor neutrons activate the surrounding materials; therefore, the neutron flux density distribution is one major focus of radiation protection. Based on TMSR-LF1 radiation safety requirements, the thermal neutron flux density outside the concrete shielding layer should be less than $1 \times 10^5 \text{ cm}^{-2} \text{ s}^{-1}$ to reduce the radiation effect caused by neutron activation [30, 31]. Gamma rays are also generated by (n, γ) reactions during the neutron absorption process. The calculation of neutron flux density distribution is necessary to analyze changes in the radiation dose rate distributions of neutrons and gamma rays. Combined with the peak distribution of neutron spectrum in the fuel region of the reactor core, the energy range of the neutron spectrum was divided into four energy segments: thermal neutron ($E \leq 0.414 \text{ eV}$), intermediate neutron ($0.414 \text{ eV} \leq E \leq 0.1 \text{ MeV}$), fast neutron ($0.1 \text{ MeV} \leq E \leq 1 \text{ MeV}$), and super-fast neutrons ($1 \text{ MeV} \leq E \leq 20 \text{ MeV}$) [32, 33]. Thermal neutrons descend at a slower pace than the other three segments in the graphite reflector; this is helpful in terms of forming a more uniform power distribution in the reactor core. The fast and super-fast neutrons ($0.1 \leq E \leq 20 \text{ MeV}$) have increased as the thermal and intermediate neutrons ($E \leq 0.1 \text{ MeV}$) are reduced quickly outside the graphite reflector (Fig. 5a). The reason for this is the presence of a 0.5-cm-thick fuel salt layer, which has large thermal neutron absorption cross sections and releases

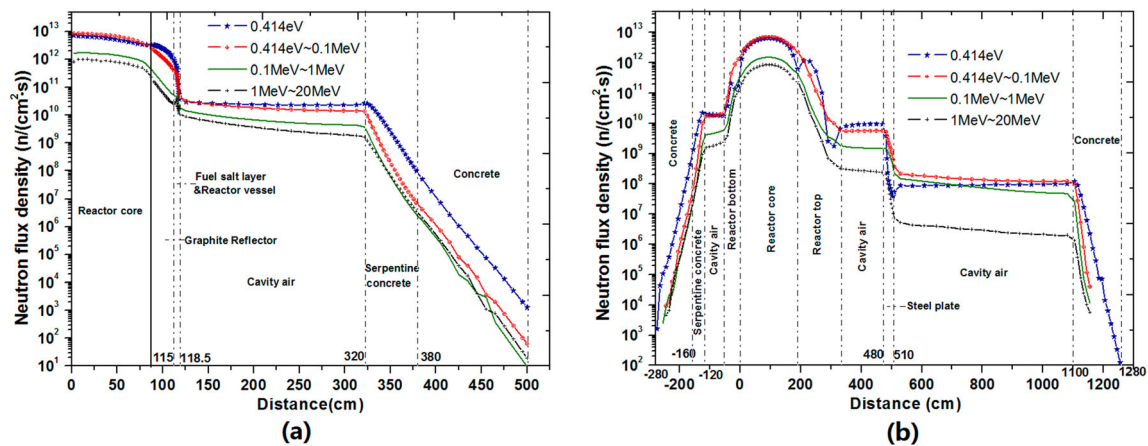


Fig. 5 (Color online) Neutron flux density distribution. **a** Radial distribution. **b** Axial distribution

high-energy neutrons after ^{235}U fission between the graphite reflector and reactor vessel. The thermal neutron flux density is higher than the fluxes of other neutrons, and therefore, thermal neutrons are the dominant component of neutrons outside the reactor vessel. When neutrons pass through the concrete shielding layer, thermal neutrons are absorbed by the concrete shielding layer, and neutrons of the other three energy segments also slow down into the thermal neutrons by the concrete shielding layer. The thermal neutron flux density outside the concrete shielding layer was still higher than the neutron flux density of the other three energy segments (Fig. 5). As the primary factor of neutron activation, the thermal neutron flux density outside the reactor shield remained the focus of attention in calculating the neutron flux density distribution.

The thermal neutron flux density distributions in serpentine concrete and ordinary concrete were determined by calculating the thermal neutron flux density corresponding to differing concrete thicknesses using tally F2. The fitted equations of the thermal neutron flux density on the side and top of the reactor with concrete thickness are expressed in Formulas (11, 12), respectively. The extrapolated thermal neutron flux density outside the ordinary concrete shield using Formula (11) was $1.89 \times 10^3 \text{ cm}^{-2} \text{ s}^{-1}$, and the extrapolated thermal neutron flux density above the ordinary concrete shielding layer with a 180 cm thickness using Formula (12) was $11 \text{ cm}^{-2} \text{ s}^{-1}$. The latter value is below the thermal neutron flux density limit of $1 \times 10^5 \text{ cm}^{-2} \text{ s}^{-1}$ for neutron activation. From Formula (11), the 10th-value layer thicknesses of the thermal neutron flux density on the side of the reactor for serpentine concrete were approximately 20.9 cm, while this value on the side of the reactor for ordinary concrete was approximately 25.6 cm. As the hydrogen content per unit volume of serpentine concrete was higher than that of ordinary concrete, serpentine concrete outperformed the ordinary concrete in terms of thermal neutron shielding. The 10th -

value layer thicknesses of the thermal neutron flux density above the top of the reactor for ordinary concrete were approximately 23.5 cm, which may be derived from Formula (12):

$$\begin{aligned} \emptyset_{\text{side}} &= 6.81 \times 10^{10} \exp(-0.11x) \times \exp(-0.09y) \\ &= 1.89 \times 10^3 \text{ cm}^{-2} \text{ s}^{-1}, \end{aligned} \quad (11)$$

$$\emptyset_{\text{top}} = 4.75 \times 10^8 \exp(-0.098h) = 11 \text{ cm}^{-2} \text{ s}^{-1}, \quad (12)$$

where x is the thickness of the serpentine concrete on the side of the reactor (60 cm); y is the thickness of ordinary concrete on the side of the reactor (120 cm); \emptyset_{side} is the thermal neutron flux density outside the reactor shield. The R^2 of Formula (11) was 0.998; h is the thickness of ordinary concrete at the top of the reactor (180 cm); \emptyset_{top} is the thermal neutron flux density above the shield on the top of the reactor, and the R^2 of Formula (12) was 0.994.

3.2 Distribution of radiation dose

The average energy of the gamma rays and that of the neutrons was 0.9 and 2 meV, respectively [14, 34, 35]. The neutrons were moderated by graphite into thermal neutrons in the reactor core, whereby most of their energy was deposited in the reactor core. The density of the graphite reflection layer was 1.86 g/cm^3 , and its shielding performance for gamma rays was low. Gamma rays were generated by (n, γ) reactions when the neutron was moderated in the graphite reflective layer, such that the gamma dose rate increases in the graphite reflective layer. The gamma dose rate increased quickly in the 0.5-cm-thick fuel salt layer as many thermal neutrons were absorbed by ^{235}U and many gamma rays were released by fission reactions (Fig. 6a). The reactor vessel made of Hastelloy-N material that was 3 cm thick demonstrated good shielding performance for neutrons and gamma (Fig. 6a). The 30-cm shielding steel plate located between the upper and lower

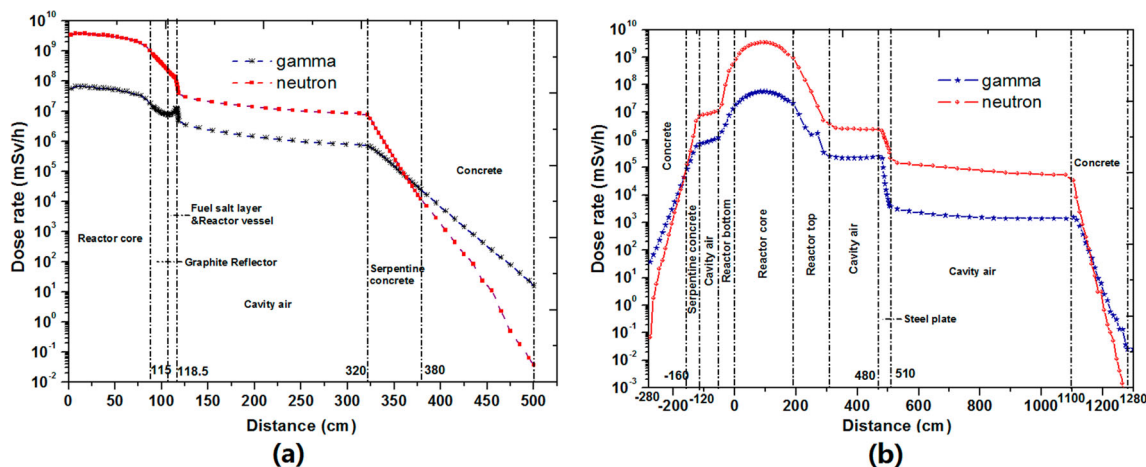


Fig. 6 (Color online) Dose rate distribution of neutron and gamma. **a** Radial distribution; **b** axial distribution

reactor regions was able to reduce the neutron and gamma dose rate of the upper region of the reactor cabin, particularly by decreasing the gamma dose rate (Fig. 6b). This effectively protects the equipment located in the upper region of the reactor cabin from excessive radiation.

The neutron dose rate was higher than the gamma dose rate inside the concrete shielding, although the neutron dose rate diminishes relatively rapidly and is lower than gamma dose rate outside the concrete shielding. The irradiation effects of gamma rays are the focus of radiation safety. The gamma dose rate was 16.1 mSv h^{-1} outside the side concrete shield, and the gamma dose rate was $1.19 \times 10^{-2} \text{ mSv h}^{-1}$ above the top concrete shield.

The neutron dose rate was much lower than the gamma dose rate outside the concrete shielding layer. From Formula (10), it was possible to extrapolate the dose rate of neutrons on the outer surface of the concrete shield facing the reactor fuel; this rate was $9.99 \times 10^{-2} \text{ mSv h}^{-1}$. From Formula (13), it was possible to extrapolate the dose rate of neutrons of the top concrete shield facing the reactor fuel; it was $6.55 \times 10^{-4} \text{ mSv h}^{-1}$.

$$D_{\text{top}} = 3 \times 10^4 \exp(-0.098h) = 6.55 \times 10^{-4} \text{ mSv h}^{-1} \tag{13}$$

where h is the thickness of ordinary concrete at the top of the reactor (180 cm); and D_{top} is the dose rate of neutrons of the ordinary concrete shield at top of the reactor, where the R^2 of the equation was 0.994.

The dose rate outside the ordinary concrete shielding layer on the side of the reactor was higher than the radiation dose rate above the ordinary concrete on the top of the reactor. This was mainly because the 30-cm shielding steel plate was set on top of the reactor, and the distance between the reactor fuel zone and the top concrete shielding layer was greater than the distance between the reactor fuel zone and the side concrete shielding layer.

Rooms around the side of the reactor were underground, and there was almost no need for people to enter during operation of the reactor. The reactor building hall was located above the concrete shielding layer on top of the reactor, and some areas of the reactor building hall required personnel to enter only for a short period of time during the operation of the reactor. The personnel entry operation requirements and radiation divisions during reactor operation were preconditions for shielding design.

4 Conclusion

This study used the MCNP5 code to calculate the neutron and gamma dose rate distributions around the TMSR-LF reactor, and the axial and radial radiation dose rate distributions of the reactor have been given, respectively. The side shielding system comprised of a 60-cm-thick thermal shield made of serpentine concrete and a 120-cm-thick primary shield made of ordinary concrete. The top shielding system comprised of a 30-cm steel platform and a 180-cm thick primary shield made of ordinary concrete. The neutron flux density followed exponential regressions in the serpentine concrete and ordinary concrete. The serpentine concrete outperformed the ordinary concrete in terms of its thermal neutron shielding performance because of the higher hydrogen content per unit volume. The thermal neutron flux density outside the shielding layer and above the ordinary concrete on top of the reactor was 1.89×10^3 and $11 \text{ cm}^{-2} \cdot \text{s}^{-1}$, respectively. The maximum thermal neutron flux density in the personnel accessible areas was below the $1 \times 10^5 \text{ cm}^{-2} \cdot \text{s}^{-1}$ limit.

The radiation dose rate in the upper region of the reactor cabin was significantly lower than that in the lower region of the reactor cabin. The 30-cm shielding steel plate was able to effectively reduce the radiation dose level around

the equipment in the upper region of the reactor cabin, thus protecting them from excessive radiation. The neutron dose rate was higher than the gamma dose rate in the concrete shielding layer of the reactor. The gamma dose rate and neutron dose rate followed exponential regressions in the serpentine concrete and ordinary concrete, whereby the neutron dose rate decreased more rapidly than the gamma dose rate in the concrete shielding layer. The gamma dose rate outside the ordinary concrete shielding layer was 16.1 mSv h^{-1} , and the neutron dose rate was $3.71 \times 10^{-2} \text{ mSv h}^{-1}$. The gamma dose rate above the ordinary concrete shield on the reactor top was $1.19 \times 10^{-2} \text{ mSv h}^{-1}$, and the neutron dose rate was $6.55 \times 10^{-4} \text{ mSv h}^{-1}$. The gamma dose rate outside the concrete shielding layer was much higher than the neutron dose rate, and the radiation dose rate of neutrons and gamma outside the concrete shielding layer was higher than the radiation dose rate on the concrete shielding layer at the top of the reactor.

The variances of all results using tally F2 and tally F5 were less than 5% when the number of simulated particles was 5×10^8 . The application of the SSW and the WWG cards with tally F2 and tally F5 was able to effectively reduce calculation time and obtain convergent calculation results.

Author contributions All authors contributed to the study conception and design. Material preparation, data collection, and analysis were performed by CYL, XBX, Jun Cai, ZHZ, GQZ, JHW, and ZCQ. The first draft of the manuscript was written by CYL, and all authors commented on previous versions of the manuscript. All authors read and approved the final manuscript.

References

- M.H. Jiang, H.J. Xu, Z.M. Dai, Advanced fission energy program-TMSR nuclear energy system. *Bull. Chin. Acad. Sci.* **27**(3), 366–374 (2012). <https://doi.org/10.3969/j.issn.1000-3045.2012.03.016>
- M.S. Cheng, Z.M. Dai, Preliminary safety analysis of molten salt breeder reactor. *Nucl. Tech.* **36**, 060601 (2013). <https://doi.org/10.11889/j.0253-3219.2013.hjs.36.060601> (in Chinese)
- S.H. Yu, Q. Sun, H. Zhao et al., Conceptual design of Mars molten salt reactor. *Nucl. Tech.* **43**(5), 050603 (2020). <https://doi.org/10.11889/j.0253-3219.2020.hjs.43.050603> (in Chinese)
- Z.M. Dai, Thorium molten salt reactor nuclear energy system (TMSR), in *Molten salt reactors and thorium energy*. ed. by T.J. Dolan (Woodhead Publishing, Cambridge, 2017), pp. 531–540
- C.Y. Zou, C.Z. Cai, C.G. Yu et al., Transition to thorium fuel cycle for TMSR. *Nucl. Eng. Des.* **330**, 420–428 (2018). <https://doi.org/10.1016/j.nucengdes.2018.01.033>
- B. Zhou, X. Yu, Y. Zou et al., Study on dynamic characteristics of fission products in 2 MW molten salt reactor. *Nucl. Sci. Tech.* **31**, 17 (2020). <https://doi.org/10.1007/s41365-020-0730-z>
- M.B. Emmett, DOMINO-II, A general purpose code for coupling DOT-IV discrete ordinates and monte carlo radiation transport calculations, ORNL/TM-7771[R]. USA: ORNL, (1981). <https://www.osti.gov/biblio/6762609>
- LANL GroupX-6. MCNP5-A General Monte Carlo Code for Neutron and Photon Transport. USAEC Report LA-7369-M, (1979)
- X-5 Monte Carlo Team, “MCNP: A general Monte Carlo N-Particle transport code, Version 5—Volume II: User’s Guide,” LA-CP-03–0245, Los Alamos National Laboratory (2008)
- Y.S. Zeng, W.G. Liu, W. Liu et al., Tritium transport analysis in a 2-MW liquid-fueled molten salt experimental reactor with the code TMSR-TTAC. *Nucl. Technol.* **205**, 582–591 (2019). <https://doi.org/10.1080/00295450.2018.1507200>
- M.A. Masoud, A.M. El-Khayatt, W.A. Kansouh et al., Insights into the effect of the mineralogical composition of serpentine aggregates on the radiation attenuation properties of their concretes. *Constr. Build. Mater.* **263**, 120141 (2020). <https://doi.org/10.1016/j.conbuildmat.2020.120141>
- K.H. Wang, F.H. Qian, Serpentine concrete in the experiment and application of Tianwan nuclear power station. *China Nucl. Power* **008**(001), 38–41 (2015). (in Chinese)
- Y.F. Liu, R. Yan, Y. Zou et al., Sensitivity/uncertainty comparison and similarity analysis between TMSR-LF1 and MSR models. *Prog. Nucl. Energy* **122**, 103289 (2020). <https://doi.org/10.1016/j.pnucene.2020.103289>
- S. Glass Tone, A. Sesonske (ed.), *Nuclear Reactor Engineering* (Third Edition) (1981), pp. 71–74. <https://doi.org/10.13182/NT82-A32943>
- R. Remetti, G. Andreoli, S. Keshishian, Monte carlo calculation of the neutron effective dose rate at the outer surface of the biological shield of HTR-10 reactor. *Nucl. Eng. Des.* **243**, 148–152 (2012). <https://doi.org/10.1016/j.nucengdes.2011.12.003>
- E.Y. Yang, L.S. Li, X.S. Chen et al., Calculation of DPA in the main components of a LBE-cooled fast reactor (BLESS-D). *Nucl. Tech.* **43**(6), 060006 (2020). <https://doi.org/10.11889/j.0253-3219.2020.hjs.43.060006> (in Chinese)
- E.E. Davidson, B.R. Betzler, D. Chandler et al., Heat deposition analysis for the high flux Isotope reactor’s HEU and LEU core models. *Nucl. Eng. Des.* **322**, 563–576 (2017). <https://doi.org/10.1016/j.nucengdes.2017.06.040>
- I. C. Gauld, O. W. Hermann, R. M. Westfall, ORIGEN-S: Scale system module to calculate fuel depletion, actinide transmutation, fission product buildup and decay, and associated radiation source terms, ORNL/TM-2005/39 Version 5.1 Vol. II, Book 1
- R.M. Ji, Y. Dai, G.F. Zhu et al., Evaluation of the fraction of delayed photoneutrons for TMSR-SF1. *Nucl. Sci. Tech.* **28**, 135 (2017). <https://doi.org/10.1007/s41365-017-0285-9>
- Y. Gong, X.C. Guan, Q. Wang et al., Design of moderator for boron neutron capture therapy based on D-D neutron source. *Nucl. Tech.* **43**(9), 090303 (2020). <https://doi.org/10.11889/j.0253-3219.2020.hjs.43.090303> (in Chinese)
- R.M. Ji, M.H. Li, Y. Zu et al., Impact of photoneutrons on reactivity measurements for TMSR-SF1. *Nucl. Sci. Tech.* **28**, 76 (2017). <https://doi.org/10.1007/s41365-017-0234-7>
- Y.W. Ma, J.G. Chen, C.G. Yu et al., Minor actinides incineration in a small modular breed and burn fast reactor. *Nucl. Technol.* **43**(9), 090602 (2020). <https://doi.org/10.11889/j.0253-3219.2020.hjs.43.090602> (in Chinese)
- Q.Y. Guo, J.Y. Zhang, Y.X. Chen, Calculation and analysis of activated corrosion products of multi-phase in water cooling loops under fusion reactor. *Nucl. Tech.* **42**(6), 60602–60602 (2019). <https://doi.org/10.11889/j.0253-3219.2019.hjs.42.060602> (in Chinese)
- G. Martín-Hernández, P.F. Mastinu, J. Praena et al., Temperature-tuned Maxwell-Boltzmann neutron spectra for kT ranging from 30 up to 50 keV for nuclear astrophysics studies. *Appl.*

- Radiat. Isot. (2012). <https://doi.org/10.1016/j.apradiso.2012.05.004>
25. H. Degenaar, M. Blaauw, The neutron energy distribution to use in Monte Carlo modeling of neutron capture in thermal neutron beams. *Nucl. Instrum. Methods Phys. Res.* **207**(2), 131–135 (2003). [https://doi.org/10.1016/S0168-583X\(03\)00457-9](https://doi.org/10.1016/S0168-583X(03)00457-9)
 26. Z.H. Zhang, X.B. Xia, J. Cai et al., Simulation of radiation dose distribution and thermal analysis for the bulk shielding of an optimized molten salt reactor. *Nucl. Sci. Tech.* **26**, 040603 (2015). <https://doi.org/10.13538/j.1001-8042/nst.26.040603>
 27. ICRP, Conversion coefficients for use in radiological protection against external radiation. ICRP Publication, (1996). <https://doi.org/10.1016/j.jnucmat.2015.01.055>
 28. S.Q. Yan, P. Cheng, G.Y. Yu et al., Design of novel lead-free flexible composites for radiation protection and simulation of protective effect. *Nucl. Tech.* **43**(5), 050201 (2020). <https://doi.org/10.11889/j.0253-3219.2020.hjs.43.050201> (in Chinese)
 29. A.O. Ezzati, M. Sohrabpour, Analysis of latent variance reduction methods in phase space Monte Carlo calculations for 6, 10 and 18 MV photons by using MCNP code. *Nucl. Instrum. Methods* **701**, 93–98 (2013). <https://doi.org/10.1016/j.nima.2012.10.089>
 30. W.F. Zhong, Y.M. Hu, Z.P. Zhong, Design and calculation for the main shielding layer of researching reactor. *J. Tsinghua Univ* **41**(2), 126–128 (2001)
 31. NB/T 20194. Design criterion of radiation shield in the PWR nuclear power plant. China: National Energy Administration, (2012)
 32. N.T. Tiep, S.M.T. Hoang, D. Hartanto et al., Investigation of the VVER-1000 reactor pressure vessel neutron fluence and displacement per atom using MCNP6. *Radiat. Phys. Chem.* **177**, 109141 (2020). <https://doi.org/10.1016/j.radphyschem.2020.109141>
 33. H.R. Vega-Carrillo, E. Manzanares-Acuña, M.P. Iñiguez et al., Spectrum of isotopic neutron sources inside concrete wall spherical cavities. *Radiat. Meas.* **42**, 1373–1379 (2007). <https://doi.org/10.1016/j.radmeas.2007.06.006>
 34. I. Stetcu, M.B. Chadwick, T. Kawano et al., Evaluation of the prompt fission gamma properties for neutron induced fission of $^{235,238}\text{U}$ and ^{239}Pu . *Nucl. Data Sheets* **163**, 261–279 (2020). <https://doi.org/10.1016/j.nds.2019.12.007>
 35. M.E. Gooden, C.W. Arnold, J.A. Becker et al., Energy dependence of fission product yields from ^{235}U , ^{238}U and ^{239}Pu for incident neutron energies between 0.5 and 14.8 MeV. *Nucl. Data Sheets* (2016). <https://doi.org/10.1016/j.nds.2015.12.006>